

# How Do Document Parsers Break? Auditing Structural Vulnerability in Document Intelligence

Yue Chen<sup>1,\*</sup>, Yihao Wang<sup>1,\*</sup>, Ziyi Tang<sup>1</sup>, Keze Wang<sup>1,†</sup>

<sup>1</sup>Sun Yat-sen University

\*Equal contribution. †Correspondence: [kezewang@gmail.com](mailto:kezewang@gmail.com)

## Abstract

Document Layout Analysis (DLA) pipelines provide structured page representations for retrieval-augmented generation, long-document question answering, and other document intelligence systems, yet their robustness evaluation remains largely area-centric. We identify this *Footprint Bias* and propose a lightweight output-level auditing framework that decouples probe construction, policy-driven targeting, and structure-aware diagnosis. The framework combines Block-level Structural Loss Rate (B-SLR), granularity-aware exposure descriptors, and pathway attribution to analyze where perturbations interact with layout structure and how failures propagate. Across MinerU and PP-StructureV3 on 1,000 pages, affected area weakly tracks perturbation-induced OCR instability ( $R^2=0.384/0.110$ ), whereas B-SLR aligns much more closely with it ( $R^2=0.727/0.916$ ). Exposure descriptors further separate occlusion- and topology-dominant pathways, and small structurally targeted probes cause downstream QA/retrieval degradation comparable to larger-footprint perturbations. These results shift DLA robustness evaluation from footprint-based stress testing toward structure-aware vulnerability auditing.

## 1 Introduction

Document Layout Analysis (DLA) converts visually organized pages into structured representations of text, tables, figures, and other layout elements. These representations serve as structural input for document intelligence systems such as retrieval-augmented generation over visually rich documents (Ueda et al., 2026), financial document reasoning (Zhao et al., 2024a), and medical record understanding (Cottet et al., 2026). Errors at this stage—including boundary corruption, spurious block merges, and misplaced outputs—can propagate as corrupted context, misaligned evidence, and unreliable downstream predictions.

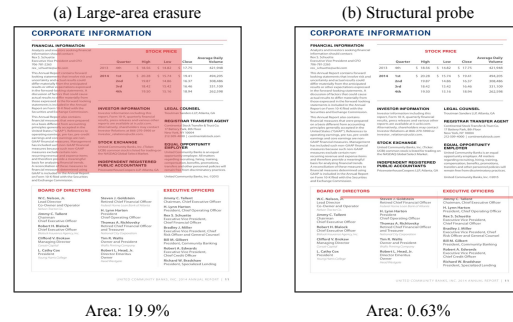


Figure 1: **Footprint Bias** in DLA robustness evaluation: (a) a large-area perturbation may cause limited error, while (b) a small structural probe can trigger greater parsing failure.

Despite progress on clean benchmarks and realistic evaluation settings, DLA robustness is still commonly assessed through aggregate degradation under corruption. Existing protocols often parameterize perturbation severity by global corruption magnitude or affected pixel footprint, while reporting damage through metrics such as CER or detection accuracy (Hendrycks and Dietterich, 2019; Michaelis et al., 2020; Chen et al., 2024; Du et al., 2025; Zhou et al., 2026). Such evaluations tell us *whether* performance declines, but reveal little about *how* or *why* parsing fails structurally. Moreover, annotation-tied diagnostics provide limited support for lightweight auditing on unlabeled document collections.

A central limitation is what we term the **Footprint Bias**: the tendency to infer perturbation severity from pixel footprint alone. As illustrated in Figure 1, small-footprint structural probes can become disproportionately damaging when they intersect sensitive layout regions. Robustness therefore depends not only on *how much* of the page is perturbed, but also on *where* the perturbation falls and *how* the failure propagates through the parsing process.

This gap motivates a more diagnostic view of DLA robustness. Since naturally occurring parser

failures are difficult to isolate and compare directly, we use controlled perturbations as counterfactual probes on real pages. Rather than asking only whether output quality deteriorates, we ask three finer-grained questions: ( $Q_1$ ) where structural identity is lost, ( $Q_2$ ) at what granularity perturbation exposure becomes predictive of failure, and ( $Q_3$ ) which pathway—direct physical occlusion or topology-level disruption—drives the degradation.

To address the resulting diagnostic problem, we propose a lightweight, output-level **tripartite auditing framework** that decouples perturbation generation from structural diagnosis. It defines a shared probe space and a policy space for attributable probe selection without modifying the audited parser, and a diagnostic space that combines observable terminal signals with structure-aware failure analysis. In particular, **Block-level Structural Loss Rate (B-SLR)** compares clean and perturbed parser outputs, enabling structural-loss auditing without manual element annotations. Experiments on two representative parsers show that structural diagnostics align with perturbation-induced OCR instability and downstream QA/retrieval failures more faithfully than footprint-based severity. Together, these results turn DLA robustness evaluation from footprint-based stress testing into structure-aware vulnerability auditing for document intelligence pipelines.

In summary, our contributions are threefold:

- We identify the **Footprint Bias**, showing that pixel footprint is an unreliable proxy for structural damage in DLA robustness evaluation.
- We propose a lightweight tripartite auditing framework that separates probe construction, policy-driven targeting, and structure-aware diagnosis.
- We instantiate the framework with B-SLR, exposure descriptors, and pathway attribution, showing that structural diagnostics better align with OCR instability and downstream QA/retrieval failures.

## 2 Related Work

**Document parsing robustness and downstream document intelligence.** Robustness evaluation has moved from generic corruption suites to document-specific parsing settings. ImageNet-C established the corruption $\times$ severity paradigm (Hendrycks and Dietterich, 2019), later extended to

detection benchmarks such as Pascal-C and COCO-C (Michaelis et al., 2020). In document parsing, RoDLA studies document-specific corruptions for DLA models (Chen et al., 2024), while DocPT-Bench and Real5-OmniDocBench extend evaluation to photographed and physically acquired documents (Du et al., 2025; Zhou et al., 2026). In parallel, document intelligence studies show that OCR and layout quality affect retrieval-augmented generation, financial document reasoning, and medical document understanding (Ueda et al., 2026; Zhao et al., 2024a; Cottet et al., 2026; Zhang et al., 2025). However, existing evaluations remain largely organized around corruption types, capture conditions, or downstream scores. They tell us whether document pipelines degrade, but provide limited explanation of which parser-level structural changes drive that degradation. Our work complements these evaluations by diagnosing structural failure mechanisms inside DLA outputs and tracing their effect on downstream QA/retrieval.

**Perturbation footprint and placement sensitivity.** Visual perturbations are often controlled by magnitude, affected area, or local patch budget. Cutout and Random Erasing use erased area as a key augmentation strength (DeVries and Taylor, 2017; Zhong et al., 2020), while document augmentation tools such as Augraphy expose visual and spatial perturbation parameters for document images (Groleau et al., 2023). Patch-based robustness studies further show that location and composition matter: adversarial patches can remain effective under small spatial budgets (Brown et al., 2017), PatchMap reveals placement hot-spots (Kimhi et al., 2025), and IMPACT jointly optimizes patch shape, location, number, and content (Yang et al., 2026). These works suggest that perturbation strength depends not only on footprint, but also on where and how perturbations interact with visual structure. Our work brings this insight to document parsing, where small perturbations can become disproportionately damaging when they interact with layout structure.

**Visual sensitivity beyond aggregate corruption.** A broader robustness literature also shows that model sensitivity cannot be fully characterized by a single global corruption score. Studies have linked robustness to frequency-dependent learning, Fourier-basis sensitivity, texture bias, and learned feature geometry (Rahaman et al., 2019; Tsuzuku and Sato, 2019; Geirhos et al., 2019; Yin et al.,

2019; Wang et al., 2020; Li et al., 2025). We do not use these mechanisms as direct explanations of document parsing failures. Rather, they motivate a diagnostic stance: robustness evaluation should identify which visual-structural factors drive failure in the target system, rather than reducing sensitivity to a single global corruption score.

### 3 Problem Setting

Let  $\mathcal{M}$  denote a document layout analysis (DLA) system that maps a document image  $I$  to a structured parsing output

$$E = \mathcal{M}(I) = \{x_i\}_{i=1}^N, \quad (1)$$

where each parsed element is represented as  $x_i = (b_i, c_i, t_i)$ , with bounding box  $b_i$ , category label  $c_i \in \mathcal{C}_5$ , and recognized text  $t_i$ . The canonical label space  $\mathcal{C}_5$  contains five layout types: text, title, table, figure, and equation.

Given a probe configuration  $P$ , detailed in Section 4, we apply a visual perturbation operator  $\mathbb{P}_P$  and obtain

$$I' = \mathbb{P}_P(I), \quad E_{\text{adv}} = \mathcal{M}(I'). \quad (2)$$

The audit evaluates the divergence between clean and perturbed parsing behavior:

$$\mathcal{A}(E, E_{\text{adv}}; P, \mathcal{Y}) = (\Delta, \mathcal{R}), \quad (3)$$

where  $\mathcal{Y}$  denotes optional benchmark references, such as ground-truth layout or text annotations when available. The terminal component  $\Delta$  records externally visible degradation signals, such as OCR CER or detection mAP drop, using  $\mathcal{Y}$  when required by the metric. These signals ground the audit in benchmark settings, but are not prerequisites for defining the structural component  $\mathcal{R}$ , which diagnoses where structural identity is lost, at what granularity perturbation exposure becomes predictive, and through which pathway failures occur. In our audit, CER is computed against the clean parser output to measure perturbation-induced OCR instability rather than absolute OCR correctness; detection degradation is measured by the per-image mAP@0.5 drop between clean and perturbed parser outputs.

Conventional robustness evaluation mainly reports  $\Delta$ . By introducing  $\mathcal{R}$ , our formulation shifts the goal from measuring aggregate degradation to diagnosing the structural effects of perturbation on the parsing process. This perturb-and-compare formulation is lightweight: it requires no parser retraining and reruns the same parser only on controlled perturbations of existing pages.

## 4 Auditing Framework

### 4.1 Tripartite Auditing Framework

As illustrated in Figure 2, we instantiate the auditing formulation with a tripartite framework:

$$\mathcal{F} = (\mathcal{S}, \Pi, \mathcal{D}), \quad (4)$$

where  $\mathcal{S}$  is a shared probe space,  $\Pi$  is a policy space for selecting probes, and  $\mathcal{D}$  is a diagnostic space for auditing the resulting parsing changes. This decomposition separates *what* perturbations can be applied, *how* they are selected for a document, and *how* their effects are measured, enabling existing parsers to be audited by changing probes or policies without modifying the parser itself.

Following Eq. 3, the diagnostic space is

$$\mathcal{D} = \Delta \times \mathcal{R}, \quad (5)$$

where  $\Delta$  denotes terminal degradation signals and  $\mathcal{R}$  denotes structure-aware diagnostic information. In Figure 2, the left side instantiates controlled perturbation through  $\mathcal{S}$  and  $\Pi$ , while the right side instantiates structural diagnosis through  $\mathcal{D}$ .

### 4.2 Controlled Perturbation

The perturbation side is designed to make naturally entangled failures attributable rather than merely observable. We abstract failure-inducing visual interactions into a shared probe space  $\mathcal{S}$  and let different policies select from it, so differences in observed damage can be attributed to selection logic rather than search-space changes.

Each probe configuration  $P \in \mathcal{S}$  is represented as

$$P = \langle \mathcal{H}, \mathcal{V}, \mathcal{B}, \mathcal{T} \rangle, \quad (6)$$

where  $\mathcal{H}$  denotes geometry,  $\mathcal{V}$  visual appearance,  $\mathcal{B}$  composition behavior, and  $\mathcal{T}$  placement strategy. Detailed probe definitions and parameter ranges are provided in Appendix A.1.

Given the shared probe space, a policy  $\pi \in \Pi$  maps available document context  $c$  to a selected probe:

$$\pi : c \mapsto \hat{P} \in \mathcal{S}. \quad (7)$$

Different policies use different levels of context, ranging from random and rule-based selection to LLM- and VLM-guided targeting. Implementation details are deferred to Appendix A.3.

### 4.3 Diagnostic Space

The diagnostic space  $\mathcal{D}$  separates *judging* from *explaining*. The terminal component  $\Delta$  records

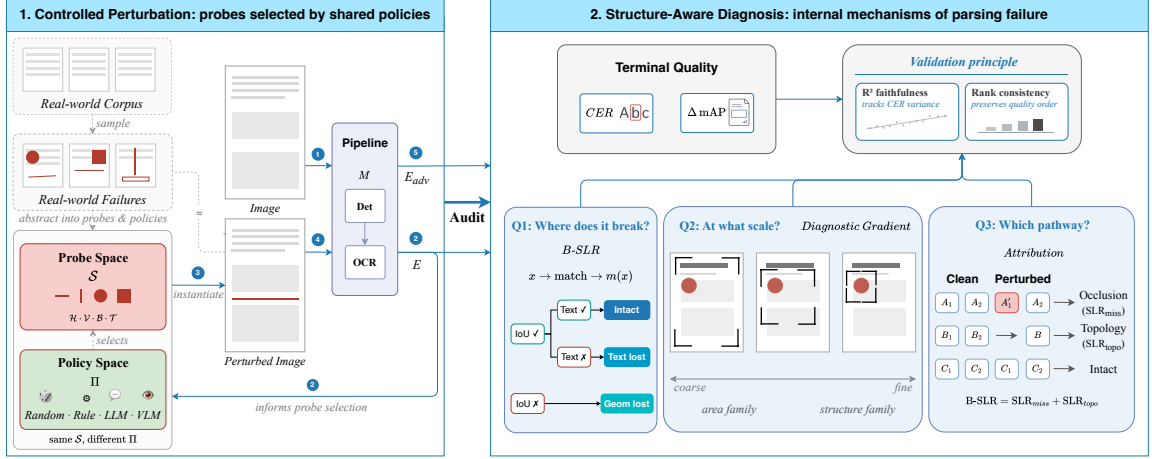


Figure 2: Overview of the proposed tripartite vulnerability auditing framework, linking controlled perturbation generation, policy-space probe selection, and diagnostic auditing.

externally visible degradation signals, while the structural component  $\mathcal{R}$  diagnoses how degradation arises inside the parsing process:

$$\Delta = (\Delta_{\text{ocr}}, \Delta_{\text{det}}), \quad \mathcal{R} = (\mathcal{R}_{\text{fail}}, \mathcal{R}_{\text{grad}}, \mathcal{R}_{\text{path}}). \quad (8)$$

We instantiate  $\Delta_{\text{ocr}}$  with OCR CER and  $\Delta_{\text{det}}$  with  $\Delta\text{mAP}$ , the per-image  $\text{mAP}@0.5$  drop between clean and perturbed parser outputs, following the metric definitions in Appendix B.4. CER serves as the primary terminal signal, while  $\Delta\text{mAP}$  provides a supplementary detection-side check. The three structural components correspond to the questions introduced in Section 1:  $\mathcal{R}_{\text{fail}}$  measures whether structural identity is lost,  $\mathcal{R}_{\text{grad}}$  describes at what granularity perturbation exposure becomes predictive of failure, and  $\mathcal{R}_{\text{path}}$  attributes failures to distinct propagation pathways.

## 4.4 Structural Diagnosis

We instantiate these three components as follows.

### 4.4.1 Structural Failure Measurement

We instantiate  $\mathcal{R}_{\text{fail}}$  by checking whether each clean parsed element preserves a valid geometry-text correspondence after perturbation. For a clean element  $x = (b, c, t) \in E$ , we assign its candidate perturbed counterpart by best-IoU lookup:

$$m(x) = \arg \max_{x' \in E_{\text{adv}}} \text{IoU}(x, x'), \quad (9)$$

where  $\text{IoU}(x, x')$  denotes box overlap.

Geometric overlap alone is insufficient, because a perturbed prediction may still overlap the correct region while losing textual identity. We therefore define text consistency as

$$\text{TextSim}(x, x') = \frac{|\text{LCS}(t(x), t(x'))|}{\max(|t(x)|, |t(x')|)}, \quad (10)$$

where LCS denotes character-level longest common subsequence. We write  $x \sim x'$  when both geometry and text are preserved:

$$x \sim x' := (\text{IoU}(x, x') \geq \tau_{\text{iou}}) \wedge (\text{TextSim}(x, x') \geq \tau_{\text{text}}), \quad (11)$$

with fixed diagnostic gates  $\tau_{\text{iou}} = 0.1$  and  $\tau_{\text{text}} = 0.5$ , where IoU admits displaced counterparts and TextSim checks textual identity; see Appendix B.5.

Using this criterion, **Block-level Structural Loss Rate (B-SLR)** is defined as

$$\mathcal{R}_{\text{fail}} := \text{B-SLR} = \frac{|\{x \in E : \neg(x \sim m(x))\}|}{|E|}. \quad (12)$$

Thus, B-SLR counts an element as structurally lost not only when its box disappears, but also when a nearby prediction remains while its textual identity is no longer preserved. Because both  $E$  and  $E_{\text{adv}}$  are parser outputs, B-SLR does not require manual element annotations and can be computed on unlabeled documents using the clean parse as the structural reference. Category corruption and topology-specific distortions are analyzed within  $\mathcal{R}_{\text{path}}$ .

### 4.4.2 Granularity-Aware Damage Descriptors

We instantiate  $\mathcal{R}_{\text{grad}}$  with five exposure descriptors that summarize how a probe interacts with page structure before terminal quality is evaluated. These descriptors span two practical settings: output-derived descriptors for reference-free auditing, and annotation-dependent descriptors for benchmark-side diagnosis when layout annotations are available. Let  $\Omega$  denote the page domain,  $S(P) \subseteq \Omega$  the perturbation support induced by probe  $P$ ,  $\Omega_L$  the union of annotated layout regions,

$\partial\Omega_L$  the corresponding boundary support,  $L$  the set of annotated layout elements, and  $E$  the clean parser output.

For any spatial support  $\Gamma \subseteq \Omega$  and any element collection  $\mathcal{X}$ , we define

$$\begin{aligned}\alpha(P; \Gamma) &= \frac{|S(P) \cap \Gamma|}{|\Gamma|}, \\ \iota(P; \mathcal{X}) &= \frac{1}{|\mathcal{X}|} \sum_{x \in \mathcal{X}} \mathbf{1}[b(x) \cap S(P) \neq \emptyset].\end{aligned}\quad (13)$$

These two operators induce the two diagnostic families:

$$\begin{aligned}\mathcal{G}_{\text{area}}(P) &= (\alpha(P; \Omega), \alpha(P; \Omega_L), \alpha(P; \partial\Omega_L)), \\ \mathcal{G}_{\text{struct}}(P) &= (\iota(P; L), \iota(P; E)).\end{aligned}\quad (14)$$

Together, these two families instantiate  $\mathcal{R}_{\text{grad}}$ . Concretely,  $\mathcal{G}_{\text{area}}$  corresponds to total occlusion ratio (TOR), area coverage ratio (ACR), and boundary pixel overlap (BPO), while  $\mathcal{G}_{\text{struct}}$  corresponds to block overlap count ratio (BOC) and element interference ratio (EIR). TOR and EIR are output-derived, whereas ACR, BPO, and BOC are annotation-dependent diagnostics used when layout annotations are available. Exact constructions of  $\Omega_L$  and  $\partial\Omega_L$  are deferred to Appendix B.1. This separation allows the core exposure analysis to remain output-level through TOR and EIR, while ACR, BPO, and BOC provide additional benchmark-side probes when annotations are available.

#### 4.4.3 Failure Pathway Attribution

We instantiate  $\mathcal{R}_{\text{path}}$  by decomposing structural failure into distinct propagation pathways. The key distinction is whether an element fails because it is directly occluded by the perturbation, or because the perturbation disrupts surrounding layout structure without heavily covering the element itself.

Let

$$\mathcal{U} = \{x \in E : \neg(x \sim m(x))\} \quad (15)$$

be the set of structurally failed elements. To quantify direct physical occlusion, we define

$$\rho(x, P) = \frac{|b(x) \cap S(P)|}{|b(x)|}. \quad (16)$$

Given an occlusion threshold  $\eta_{\text{occ}} = 0.3$ , the failure set is partitioned as

$$\begin{cases} \mathcal{U}_{\text{miss}} = \{x \in \mathcal{U} : \rho(x, P) \geq \eta_{\text{occ}}\}, \\ \mathcal{U}_{\text{topo}} = \{x \in \mathcal{U} : \rho(x, P) < \eta_{\text{occ}}\}. \end{cases} \quad (17)$$

The corresponding normalized pathway losses are

$$\text{SLR}_{\text{miss}} = \frac{|\mathcal{U}_{\text{miss}}|}{|E|}, \quad \text{SLR}_{\text{topo}} = \frac{|\mathcal{U}_{\text{topo}}|}{|E|}. \quad (18)$$

By construction,

$$\text{B-SLR} = \text{SLR}_{\text{miss}} + \text{SLR}_{\text{topo}}.$$

We instantiate  $\mathcal{R}_{\text{path}} = (\text{SLR}_{\text{miss}}, \text{SLR}_{\text{topo}})$ , with the topology-dominant subset further resolved into merge, misclass, and degraded errors.

Within  $\mathcal{U}_{\text{topo}}$ , we further assign each failure to one of three layout-aware types: *merge*, where multiple clean elements collapse into the same perturbed prediction; *misclass*, where spatial correspondence is largely preserved but the canonical category changes; and *degraded*, which covers the remaining non-occlusion failures. We apply the priority order  $\text{merge} > \text{misclass} > \text{degraded}$ , yielding a disjoint and exhaustive partition of  $\mathcal{U}_{\text{topo}}$ . Full definitions are given in Appendix B.1.

## 4.5 Validation Principle

The structural diagnostics in  $\mathcal{R}$  are useful only if they remain grounded in terminal degradation signals. We validate this grounding from two perspectives. First, *faithfulness* measures whether a structural variable tracks perturbation-induced OCR instability:

$$\text{Faith}(X) = R^2(\overline{X}, \overline{\text{CER}}), \quad (19)$$

where overlines denote configuration-level means and  $R^2$  denotes the coefficient of determination. Second, *ranking consistency* checks whether structural diagnostics preserve the vulnerability ordering suggested by terminal judges such as CER and  $\Delta\text{mAP}$ . Together, these criteria ensure that  $\mathcal{R}$  provides externally meaningful explanations rather than merely internally defined scores.

## 5 Experiments

### 5.1 Experimental Setup

We instantiate  $\mathcal{F} = (\mathcal{S}, \Pi, \mathcal{D})$  on 1,000 validation pages from PubLayNet (Zhong et al., 2019) and DocLayNet (Pfitzmann et al., 2022), after filtering pages with fewer than five original spans.

**Audited pipelines.** We audit two parsers that expose block-level boxes and recognized text: **MinerU v2.7.6** (Wang et al., 2024), based on DocLayout-YOLO (Zhao et al., 2024b) with separate recognition modules, and **PP-StructureV3** (Cui et al., 2025), a cascaded Pad-

dleOCR pipeline using RT-DETR-H and PaddleOCR 3.x. Both are evaluated under the same B-SLR matching thresholds ( $\tau_{\text{iou}} = 0.1$ ,  $\tau_{\text{text}} = 0.5$ ). End-to-end VLM parsers are excluded because they do not expose the box-text outputs required by  $\mathcal{D}$ . Annotations are used only for sampling, detection metrics, and annotation-dependent exposure descriptors.

**Auditing protocols.** We use two complementary protocols. **Phase 1** performs fixed-configuration auditing by traversing 29 probe configurations in  $\mathcal{S}$ , yielding 29,000 records per pipeline. **Phase 2** performs policy-driven auditing by comparing five policy families—random, rule-based, LLM-biased, LLM-neutral, and VLM strategy-only—over the same page pool and shared probe space. Configuration identifiers and policy details are provided in Appendices C.1 and A.3.

**Statistical protocol.** The main text reports configuration-level analyses, with image fixed-effects regression, per-image OLS, Spearman analysis, dose-response binning, and within-configuration quantile checks reported in Appendix C.6.

Setting	MinerU	PP-V3
Input images / valid pages	1,000	1,000
Shared evaluation pool		1,000
Complexity (S / M / C)	14.5% / 46.4% / 39.1%	
Phase 1 configs / Phase 2 policies		29 / 5
Matching thresholds	$\tau_{\text{iou}} = 0.1$ , $\tau_{\text{text}} = 0.5$	

Table 1: Dataset and protocol summary.

## 5.2 Results and Analysis

We first quantify the Footprint Bias at the parser level and test whether the same mismatch propagates to downstream QA and evidence retrieval. We then diagnose the structural mechanisms behind it through B-SLR channels, pathway-specific exposure descriptors, probe-family sensitivity, and policy-driven targeting.

### 5.2.1 Footprint Bias Quantification

Figure 3 tests whether affected area is a reliable severity proxy for perturbation-induced OCR instability. It is not: TOR explains CER only weakly on MinerU ( $R^2=0.384$ ) and almost not at all on PP-StructureV3 ( $R^2=0.110$ ). Even within the matched-TOR region, configurations with comparable footprint exhibit a CER spread of roughly  $2.7\times$ , showing that footprint alone cannot deter-

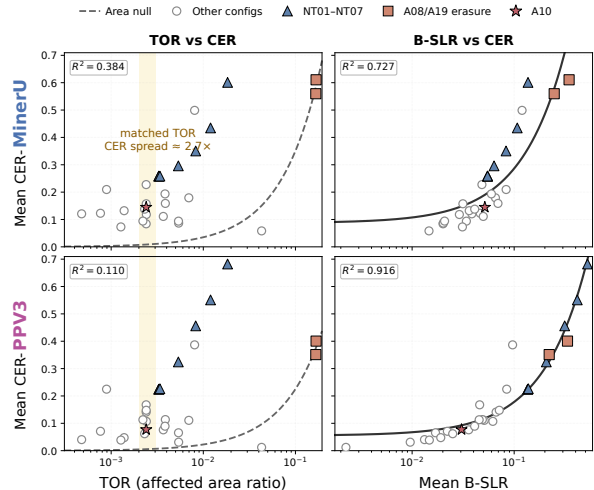


Figure 3: Configuration-level means ( $n=29$ ) show that B-SLR aligns with perturbation-induced OCR instability substantially better than affected area in both parsers; higher CER and B-SLR indicate greater OCR instability and structural loss.

mine whether a perturbation is structurally harmful.

By contrast, realized structural loss measured by B-SLR is much more aligned with the terminal OCR signal, with  $R^2=0.727$  on MinerU and  $0.916$  on PP-StructureV3. Configurations that appear anomalous under a footprint-only view return to the fitted trend once structural loss is considered. Thus, the failure signal is not explained by how much area is perturbed alone, but by whether the perturbation breaks parser-visible structure.

### 5.2.2 Downstream Impact

**Table 2: Downstream propagation.** All values are percentages; EM Drop and AnsMiss are lower-better degradation signals, while EM and AnsHit@5 are higher-better task scores; AM/Str./LA denote area-matched/structural/large-area; bold marks the more degraded AM-Str. result.

Parser	Cond.	TOR	EM $\uparrow$	EM Drop $\downarrow$	AnsMiss $\downarrow$	BM25	AnsHit@5 $\uparrow$	Dense	AnsHit@5 $\uparrow$
MinerU	Clean	0.00	63.5	–	0.0		94.6		93.6
	AM	0.10	63.1	0.4	1.1		93.8		92.8
	Str.	0.11	56.2	<b>7.3</b>	<b>13.7</b>		<b>81.0</b>		<b>80.4</b>
	LA	16.61	38.8	24.7	36.8		58.8		59.4
PP-V3	Clean	0.00	63.6	–	0.0		94.7		95.1
	AM	0.10	63.1	0.5	2.3		92.9		93.4
	Str.	0.11	58.1	<b>5.5</b>	<b>12.2</b>		<b>83.1</b>		<b>83.5</b>
	LA	16.61	38.4	25.2	39.6		57.9		58.7

Table 2 reports a controlled propagation test for downstream document use. Rather than introducing a separate document-QA benchmark, we reuse the same 975 clean-derived QA pairs under four counterfactual parser outputs, so that only the perturbation condition changes. For retrieval, the corpus is restricted to chunks from the same page and uses the same block-aware chunking across all conditions; this isolates whether answer-bearing

evidence remains available after parsing. The key contrast controls for visual footprint: area-matched erasure (AM) and the structural probe (Str.) perturb nearly the same page area, with TOR around 0.10–0.11%.

Under this matched footprint, AM remains close to the clean condition, whereas Str. consistently damages both answering and evidence retrieval. Across the two parsers, Str. increases EM Drop to 5.5–7.3 points, raises answer-missing rates to 12–14%, and lowers BM25/Dense Hit@5 from above 92% to roughly 80–84%. LA causes the largest absolute degradation, but with about  $150\times$  larger footprint. Thus, downstream failure follows structural interaction rather than footprint alone: a small structure-targeted probe can remove or disorganize answer-bearing evidence even when an area-matched erasure barely affects the task.

### 5.2.3 B-SLR Channels and Faithfulness

	(a) Channel partition			(b) Cross-channel coupling			
	B-SLR	IoU	text		$\rho_s$	$R^2_{\text{IoU}}$	$R^2_{\text{text}}$
MinerU	.071	.028	<b>.043</b>	MinerU	.891	<b>.927</b>	.893
PP-V3	.111	.026	<b>.085</b>	PP-V3	.380	.186	<b>.900</b>

Table 3: Configuration-level B-SLR channel decomposition ( $n=29$ ): mean channel losses and cross-channel coupling ( $\rho_s$  for IoU–text rank correlation;  $R^2$  columns are univariate OLS channel–CER fits across configuration means).

Returning to the parser-level diagnostic, we next examine whether composite B-SLR is internally decomposable. Under the joint IoU+text criterion, each failed element is assigned to either an IoU-fail channel, where no valid geometric match survives, or a text-fail-only channel, where geometry is retained but textual identity is lost. The two channels sum to composite B-SLR, and Table 3 reports their configuration-level means and coupling statistics over the 29 Phase 1 configurations.

The decomposition reveals two patterns. First, text-side failure is non-redundant and dominant in both pipelines: its mean contribution exceeds the IoU channel on MinerU (.043 vs. .028) and more strongly on PP-V3 (.085 vs. .026). Thus, many structural failures preserve coarse geometry while losing recognized content. Second, the channel coupling differs sharply across architectures. MinerU shows coherent geometry-text variation ( $\rho_s = .891$ ), whereas PP-V3 is driven mainly by the text channel ( $R^2_{\text{text}} = .900$  vs.  $R^2_{\text{IoU}} = .186$ ). This suggests that PP-V3 concentrates vulnerabil-

ity in recognition-side failure, while MinerU distributes failure across both geometry and text.

These channel-level differences also clarify how B-SLR should be interpreted. Because CER measures perturbation-induced text instability, the text channel is expected to be informative; the useful observation is that the geometry–text coupling differs sharply by architecture rather than collapsing to a single text-only score. Composite B-SLR therefore serves as an output-level structural diagnostic aligned with the terminal OCR-instability signal, reaching  $R^2 = .727/.916$  and Spearman  $\rho = .911/.973$  on MinerU/PP-V3.

### 5.2.4 Gradient Predicts Failure Pathways

Pipeline	Pathway	$\mathcal{G}_{\text{area}}$			$\mathcal{G}_{\text{struct}}$	
		TOR	ACR	BPO	BOC	EIR
MinerU	SLR <sub>miss</sub>	.927	.907	<b>.964</b>	.071	.044
	SLR <sub>topo</sub>	.004	.005	.003	.610	<b>.623</b>
PP-V3	SLR <sub>miss</sub>	.916	.895	<b>.960</b>	.072	.073
	SLR <sub>topo</sub>	.009	.008	.008	<b>.708</b>	.702

Table 4: Configuration-level  $R^2$  ( $n=29$ ) from univariate OLS fits between each diagnostic descriptor and pathway loss. Bold marks the strongest predictor per row.

We next ask which exposure granularity predicts each failure pathway. Table 4 regresses the two pathway losses, SLR<sub>miss</sub> and SLR<sub>topo</sub>, on the five diagnostic descriptors, grouped into the area family  $\mathcal{G}_{\text{area}} = (\text{TOR}, \text{ACR}, \text{BPO})$  and the structure family  $\mathcal{G}_{\text{struct}} = (\text{BOC}, \text{EIR})$ .

The specialization is consistent across both pipelines. For SLR<sub>miss</sub>, BPO is the strongest predictor ( $R^2=0.964/0.960$  on MinerU/PP-V3), with TOR and ACR also high but weaker. For SLR<sub>topo</sub>, the pattern reverses: area-family descriptors drop near zero, whereas BOC/EIR dominate ( $R^2=0.610/0.623$  on MinerU and  $0.708/0.702$  on PP-V3). Thus, the two descriptor families are not interchangeable severity measures: boundary-sensitive area exposure predicts direct occlusion, while element-level structural interference predicts topology-dominant loss.

This addresses Q<sub>2</sub>: footprint becomes informative only after being refined by structural contact. As exposure descriptors computed before terminal scoring, BPO and EIR indicate different risks: boundary overlap signals direct occlusion, while element interference signals topology-dominant disruption. The NT sweep in Section 5.2.5 exemplifies this regime, increasing structural interference without a matched increase in TOR. A ranking-

Parser	Policy	Exposure / Budget				Terminal & Structural Damage			Failure Pathway			Efficiency	
		TOR	BPO	BOC	EIR	CER (err.) $\uparrow$	$\Delta$ mAP (drop) $\uparrow$	B-SLR (loss) $\uparrow$	SLR <sub>miss</sub>	SLR <sub>topo</sub>	TopoShare	Eff <sub>B-SLR</sub> $\uparrow$	Eff <sub>CER</sub> $\uparrow$
MinerU	Random	.035	.050	.331	.357	.226	.043	.088	.018	.070	.82	10.9	24.5
	Rule-based	.005	.015	.292	.352	.245	.048	.077	.000	.077	1.00	23.8	61.4
	LLM-biased	.006	.026	.157	.182	.177	.025	.068	.003	.065	.94	16.0	35.7
	LLM-neutral	.008	.011	.125	.145	.209	.034	.058	.003	.055	.91	12.2	40.2
	VLM	.003	.007	.099	.124	.176	.014	.056	.000	.056	1.00	<b>25.3</b>	<b>73.3</b>
PP-V3	Random	.035	.050	.331	.312	.227	.026	.077	.013	.064	.80	9.1	22.1
	Rule-based	.005	.015	.292	.312	.230	.037	.077	.001	.076	.98	<b>17.6</b>	<b>33.3</b>
	LLM-biased	.007	.027	.155	.125	.123	.012	.049	.003	.046	.88	9.4	18.1
	LLM-neutral	.008	.012	.127	.129	.119	.024	.048	.004	.044	.83	10.7	20.5
	VLM	.003	.007	.104	.092	.081	.005	.034	.000	.033	.98	15.9	30.5

Table 5: **Phase 2 policy audit.**  $\Delta$ mAP =  $mAP(\mathcal{Y}, E) - mAP(\mathcal{Y}, E_{adv})$ ; TopoShare =  $SLR_{topo} / (SLR_{miss} + SLR_{topo})$ ; Eff<sub>B-SLR</sub> = B-SLR/TOR, Eff<sub>CER</sub> = CER/TOR.  $\uparrow$ : denotes larger per-footprint efficiency

consistency check against CER yields the same family-level ordering, indicating that the specialization is not an artifact of B-SLR alone.

### 5.2.5 Sensitivity Across Probe Families

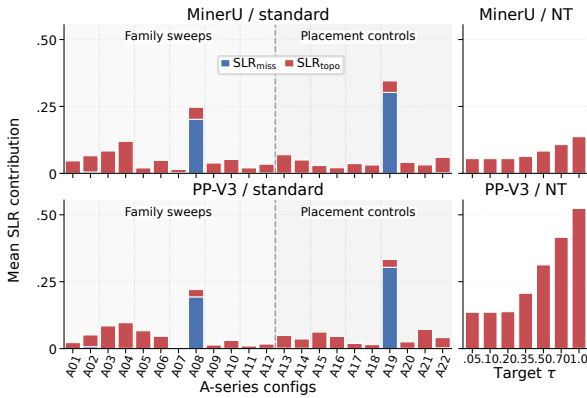


Figure 4: **Phase 1 pathway decomposition.** Bars decompose B-SLR into SLR<sub>miss</sub> and SLR<sub>topo</sub>; higher bars indicate greater structural loss, and configuration identifiers are decoded in Appendix C.1.

Figure 4 reports the Phase 1 fixed-configuration audit, where the targeting rule is fixed and variation mainly reflects probe-level effects. Damage is highly concentrated: the largest A-series spikes appear at A08 and A19 for both pipelines, indicating that severe erasure-style probes are disproportionately destructive, while most other configurations remain much weaker. The dominant pathway also varies by configuration: extreme erasure is largely miss-driven, whereas many non-extreme configurations are dominated by SLR<sub>topo</sub>, indicating topology-level disruption rather than direct element removal.

The NT sweep further reveals parser-dependent sensitivity to sustained structural interference. MinerU increases gradually as the target interference level  $\tau$  grows, whereas PP-StructureV3 shows a steeper rise in topology-dominant loss at higher target levels. Overall, Phase 1 shows that the probe space contains qualitatively different failure regimes: severe erasure produces miss-

heavy spikes, while structure-targeted interference increasingly induces topology-dominant failure.

### 5.2.6 Targeting Efficiency Across Policies

Table 5 reports the Phase 2 policy-driven audit, where all policies share the same probe space  $\mathcal{S}$  and page pool. We use these policies not as competing attacks, but as probes of whether targeting logic can expose structural damage under different area budgets.

The results reinforce the footprint-bias finding under policy-level selection. Structurally targeted policies often reach comparable structural loss with much smaller area budgets: for example, Rule-based matches Random on PP-V3 B-SLR despite using about one seventh of the TOR, and exceeds Random on MinerU CER with a similarly small budget. Thus, policy choice changes not only how much area is perturbed, but whether the selected area is structurally consequential.

The pathway decomposition shows that this efficiency is not mainly direct content removal. TopoShare remains high (.80–1.00), and SLR<sub>miss</sub> is near zero for most non-random policies. Absolute damage and per-footprint efficiency therefore expose complementary aspects of vulnerability: Random can produce larger raw damage by spending more area, whereas targeted policies reveal structure-sensitive failure per unit footprint.

## 6 Conclusion

We introduced a lightweight, output-level tripartite auditing framework for structure-aware DLA vulnerability auditing. Across MinerU and PP-StructureV3, B-SLR tracks OCR instability more faithfully than footprint, exposure descriptors separate occlusion- and topology-dominant pathways, and targeted probes reveal disproportionate downstream QA/retrieval degradation under small area budgets. Overall, DLA reliability should be evaluated structurally, not by footprint alone.

## Limitations

This work focuses on diagnostic auditing rather than universal robustness certification. First, our experiments cover two representative DLA pipelines with different detection and recognition designs. This setting is sufficient to expose cross-architecture differences, but broader coverage across additional parsers, detector families, and end-to-end document models would further test the generality of the observed diagnostic patterns. Second, our framework requires block-level boxes and recognized text, so systems that expose only free-form textual outputs or latent structured representations require an additional alignment interface before they can be audited in the same way. Third, our mechanistic interpretation is based on controlled black-box interventions and output-level diagnostics. While this is appropriate for pipeline-level auditing, white-box analyses of detector and recognizer internals would be needed to localize the exact feature-level causes of failure. Fourth, per-pixel efficiency metrics such as B-SLR/TOR are most informative when comparing probes within comparable area ranges; they should be interpreted together with absolute damage and pathway composition. Finally, although the evaluation pool combines PubLayNet and DocLayNet pages, dataset-specific annotation conventions may affect absolute scores, and larger cross-domain audits remain an important extension.

**Future work.** Future work can extend the audit to more parser families, develop adapters for end-to-end or generative document parsers, and connect structural diagnostics with downstream tasks such as retrieval-augmented document question answering.

## Ethics Statement

This work studies vulnerability auditing for defensive robustness evaluation. We report attack-like procedures solely to improve safety testing and mitigation in document intelligence systems.

## Reproducibility Statement

We specify probe families, the matching protocol, and evaluation metrics in equations and tables; figure paths in the source repository correspond to the plots reported here.

## References

- Youngmin Baek, Daehyun Nam, Sungrae Park, Junyeop Lee, Seung Shin, Jeonghun Baek, Chae Young Lee, and Hwalsuk Lee. 2020. Clevel: Character-level evaluation for text detection and recognition tasks. In *Proceedings of the IEEE/CVF Conference on Computer Vision and Pattern Recognition (CVPR) Workshops*.
- Tom B Brown, Dandelion Mané, Aurko Roy, Martín Abadi, and Justin Gilmer. 2017. Adversarial patch. *arXiv preprint arXiv:1712.09665*.
- Yufan Chen, Jiaming Zhang, Kunyu Peng, Junwei Zheng, Ruiping Liu, Philip Torr, and Rainer Stiefelhagen. 2024. Rodla: Benchmarking the robustness of document layout analysis models. In *Proceedings of the IEEE/CVF Conference on Computer Vision and Pattern Recognition (CVPR)*, pages 15556–15566.
- Jonathan Pattin Cottet, Véronique Eglin, and Alex Aussem. 2026. [Lightweight domain-specific language model for real-time structuring of medical prescriptions](#). In *Proceedings of the 19th Conference of the European Chapter of the Association for Computational Linguistics (Volume 5: Industry Track)*, pages 915–926, Rabat, Morocco. Association for Computational Linguistics.
- Cheng Cui, Ting Sun, Manhui Lin, Tingquan Gao, Yubo Zhang, Jiakuan Liu, Xueqing Wang, Zelun Zhang, Changda Zhou, Hongen Liu, Yue Zhang, Wenyu Lv, Kui Huang, Yichao Zhang, Jing Zhang, Jun Zhang, Yi Liu, Dianhai Yu, and Yanjun Ma. 2025. [Paddleocr 3.0 technical report](#). *Preprint*, arXiv:2507.05595.
- Terrance DeVries and Graham W. Taylor. 2017. [Improved regularization of convolutional neural networks with cutout](#). *Preprint*, arXiv:1708.04552.
- Yongkun Du, Pinxuan Chen, Xuye Ying, and Zhineng Chen. 2025. [Docptbench: Benchmarking end-to-end photographed document parsing and translation](#). *Preprint*, arXiv:2511.18434.
- Robert Geirhos, Patricia Rubisch, Claudio Michaelis, Matthias Bethge, Felix A. Wichmann, and Wieland Brendel. 2019. [Imagenet-trained CNNs are biased towards texture; increasing shape bias improves accuracy and robustness](#). In *International Conference on Learning Representations*.
- Alexander Groleau, Kok Wei Chee, Stefan Larson, Samay Maini, and Jonathan Boorman. 2023. Augraphy: A data augmentation library for document images. In *Document Analysis and Recognition - IC-DAR 2023*, pages 384–401, Cham. Springer Nature Switzerland.
- Dan Hendrycks and Thomas Dietterich. 2019. [Benchmarking neural network robustness to common corruptions and perturbations](#). In *International Conference on Learning Representations*.

- Shai Kimhi, Moshe Kimhi, and Avi Mendelson. 2025. Benchmarking adversarial patch selection and location. *Mathematics*, 14(1):103.
- Chae Young Lee, Youngmin Baek, and Hwalsuk Lee. 2019. [Tedeval: A fair evaluation metric for scene text detectors](#). In *2019 International Conference on Document Analysis and Recognition Workshops (ICDARW)*, volume 7, pages 14–17.
- Binghui Li, Zhixuan Pan, Kaifeng Lyu, and Jian Li. 2025. [Feature averaging: An implicit bias of gradient descent leading to non-robustness in neural networks](#). In *The Thirteenth International Conference on Learning Representations*.
- Claudio Michaelis, Benjamin Mitzkus, Robert Geirhos, Evgenia Rusak, Oliver Bringmann, Alexander S. Ecker, Matthias Bethge, and Wieland Brendel. 2020. [Benchmarking robustness in object detection: Autonomous driving when winter is coming](#).
- Birgit Pfitzmann, Christoph Auer, Michele Dolfi, Ahmed S. Nassar, and Peter Staar. 2022. [Doclaynet: A large human-annotated dataset for document-layout segmentation](#). In *Proceedings of the 28th ACM SIGKDD Conference on Knowledge Discovery and Data Mining, KDD '22*, pages 3743–3751, New York, NY, USA. Association for Computing Machinery.
- Nasim Rahaman, Aristide Baratin, Devansh Arpit, Felix Draxler, Min Lin, Fred Hamprecht, Yoshua Bengio, and Aaron Courville. 2019. [On the spectral bias of neural networks](#).
- Yusuke Tsuzuku and Issei Sato. 2019. [On the structural sensitivity of deep convolutional networks to the directions of fourier basis functions](#). In *Proceedings of the IEEE/CVF Conference on Computer Vision and Pattern Recognition (CVPR)*.
- Nobuhiro Ueda, Yuyang Dong, Krisztián Boros, Daiki Ito, Takuya Sera, and Masafumi Oyamada. 2026. [SCAN: Semantic document layout analysis for textual and visual retrieval-augmented generation](#). In *Findings of the Association for Computational Linguistics: EACL 2026*, pages 1618–1637, Rabat, Morocco. Association for Computational Linguistics.
- Bin Wang, Chao Xu, Xiaomeng Zhao, Linke Ouyang, Fan Wu, Zhiyuan Zhao, Rui Xu, Kaiwen Liu, Yuan Qu, Fukai Shang, Bo Zhang, Liqun Wei, Zhihao Sui, Wei Li, Botian Shi, Yu Qiao, Dahua Lin, and Conghui He. 2024. [Mineru: An open-source solution for precise document content extraction](#). *Preprint*, arXiv:2409.18839.
- Haohan Wang, Xindi Wu, Zeyi Huang, and Eric P. Xing. 2020. [High-frequency component helps explain the generalization of convolutional neural networks](#). In *Proceedings of the IEEE/CVF Conference on Computer Vision and Pattern Recognition (CVPR)*.
- Zenghui Yang, Xingquan Zuo, Hai Huang, Gang Chen, Xinchao Zhao, and Tianle Zhang. 2026. [IMPACT: Irregular multi-patch adversarial composition based on two-phase optimization](#). In *The Thirty-ninth Annual Conference on Neural Information Processing Systems*.
- Dong Yin, Raphael Gontijo Lopes, Jon Shlens, Ekin Dogus Cubuk, and Justin Gilmer. 2019. [A fourier perspective on model robustness in computer vision](#). In *Advances in Neural Information Processing Systems*, volume 32. Curran Associates, Inc.
- Junyuan Zhang, Qintong Zhang, Bin Wang, Linke Ouyang, Zichen Wen, Ying Li, Ka-Ho Chow, Conghui He, and Wentao Zhang. 2025. [Ocr hinders rag: Evaluating the cascading impact of ocr on retrieval-augmented generation](#). In *Proceedings of the IEEE/CVF International Conference on Computer Vision (ICCV)*, pages 17443–17453.
- Yilun Zhao, Yitao Long, Hongjun Liu, Ryo Kamoi, Linyong Nan, Lyuhao Chen, Yixin Liu, Xiangru Tang, Rui Zhang, and Arman Cohan. 2024a. [DocMath-eval: Evaluating math reasoning capabilities of LLMs in understanding long and specialized documents](#). In *Proceedings of the 62nd Annual Meeting of the Association for Computational Linguistics (Volume 1: Long Papers)*, pages 16103–16120, Bangkok, Thailand. Association for Computational Linguistics.
- Zhiyuan Zhao, Hengrui Kang, Bin Wang, and Conghui He. 2024b. [Doclayout-YOLO: Enhancing document layout analysis through diverse synthetic data and global-to-local adaptive perception](#).
- Xu Zhong, Jianbin Tang, and Antonio Jimeno Yepes. 2019. [Publaynet: Largest dataset ever for document layout analysis](#). In *2019 International Conference on Document Analysis and Recognition (ICDAR)*, pages 1015–1022.
- Zhun Zhong, Liang Zheng, Guoliang Kang, Shaozi Li, and Yi Yang. 2020. [Random erasing data augmentation](#). In *Proceedings of the AAAI conference on artificial intelligence*, pages 13001–13008.
- Changda Zhou, Ziyue Gao, Xueqing Wang, Tingquan Gao, Cheng Cui, Jing Tang, and Yi Liu. 2026. [Real5-omnidocbench: A full-scale physical reconstruction benchmark for robust document parsing in the wild](#). *Preprint*, arXiv:2603.04205.

## A Implementation Details of Probe and Policy Spaces

### A.1 Probe Space and Probe Catalog

Each probe configuration is specified by four dimensions:

$$P = \langle \mathcal{H}, \mathcal{V}, \mathcal{B}, \mathcal{T} \rangle, \quad (20)$$

where  $\mathcal{H}$  denotes geometry,  $\mathcal{V}$  visual appearance,  $\mathcal{B}$  composition behavior, and  $\mathcal{T}$  placement strategy. This factorization keeps the perturbation space

modular: probe geometry, visual appearance, composition behavior, and placement can be controlled or varied while all policies draw from the same admissible space.

Table 6 summarizes the probe catalog used throughout the audit. The catalog covers line-like artifacts, area erasures, local overlays, point clusters, and irregular patches, so that the shared probe space contains both footprint-heavy and structure-sensitive perturbations. Figure 5 visualizes representative examples of these probe families.

## A.2 Probe Generation and Placement

This subsection specifies how the probe catalog in Table 6 is rendered on a document page. We denote geometry masks by  $\mathcal{H}_{(\cdot)}$  to distinguish probe geometry from the diagnostic gradient families in the main text. The geometry primitives are implemented as binary masks:

$$\mathcal{H}_{\text{line}}(\theta, l, w) = \{(x, y) : |x \sin \theta - y \cos \theta| < \frac{w}{2}, \\ 0 \leq x \cos \theta + y \sin \theta \leq l\}, \quad (21)$$

$$\mathcal{H}_{\text{disk}}(r) = \{(x, y) : x^2 + y^2 \leq r^2\}, \quad (22)$$

$$\mathcal{H}_{\text{rect}}(w_r, h_r) = \{(x, y) : |x| \leq w_r/2, |y| \leq h_r/2\}, \quad (23)$$

$$\mathcal{H}_{\text{blob}}(r_b, \epsilon) = \{(r, \phi) : r \leq r_b(1 + \epsilon \cdot \text{Perlin}(\phi))\}, \quad (24)$$

$$\mathcal{H}_{\text{point}}(n, r, \sigma) = \bigcup_{i=1}^n \mathcal{H}_{\text{disk}}(r) \Big|_{\text{center} \sim \mathcal{N}(\mu, \sigma^2 I)}. \quad (25)$$

Appearance families include solid color, gradient, ring, and procedural texture. All probe actions are unified by alpha blending:

$$I'(x, y) = (1 - \alpha(x, y))I(x, y) + \alpha(x, y)t(x, y), \quad (26)$$

where  $t(x, y)$  is the probe texture or background target. The three composition behaviors in Table 6 are instantiated as *inject* ( $\alpha = 1$ ), *blend* ( $\alpha \in (0, 1)$ ), and *erase* (blending toward the local background color).

Placement strategies are defined over content and boundary masks derived from the clean-layout boxes. Let  $\{b_i\}$  denote clean-layout boxes and  $\partial b_i$  their boundaries. The anchor region is

$$M_{\text{anchor}} = \mathcal{D} \left( \bigcup_i \partial b_i, \delta \right) \setminus M_{\text{content}}^{\text{erode}(\delta)}, \quad (27)$$

where  $\delta = 5$  px (Appendix B.5). We use four placement strategies: **anchor** (a, on  $M_{\text{anchor}}$ ), **content** (c, inside  $M_{\text{content}}$ ), **random** (r, uniformly over

the page), and **bridge** (b, at the midpoint between two neighboring blocks). Across experiments, one to three probes are placed per page under a global area budget.

## A.3 Policy Families

The policy space  $\Pi$  maps page context to a probe configuration in the shared probe space of Table 6. Formally, each policy is written as

$$\pi : c \mapsto \hat{P} = \langle \hat{\mathcal{H}}, \hat{\mathcal{V}}, \hat{\mathcal{B}}, \hat{\mathcal{T}} \rangle, \quad (28)$$

where  $c$  denotes context features extracted from the current page, and  $\hat{P}$  follows the same geometry–appearance–behavior–placement schema as Section A.1.

We use five non-iterative policy families under the identical probe space:

- **Random** ( $\pi_{\text{rand}}$ ): uniformly samples the probe type, parameters, and placement strategy.
- **Rule-based** ( $\pi_{\text{rule}}$ ): selects probes using boundary density and inter-block gap heuristics.
- **LLM-biased** ( $\pi_{\text{LLM}}^{\text{biased}}$ ): uses a language-guided prompt with explicit structural hints.
- **LLM-neutral** ( $\pi_{\text{LLM}}^{\text{neutral}}$ ): uses a language-guided prompt without explicit structural hints.
- **VLM strategy-only** ( $\pi_{\text{VLM}}$ ): predicts probe type and placement strategy from the page image without direct coordinate output.

All policies emit the same schema—probe type, parameters, and placement strategy—so differences in observed damage can be attributed to targeting logic rather than search-space mismatch.

## A.4 Controlled Prompt Design

The biased and neutral LLM prompts are controlled variants designed to test whether structural targeting is driven by explicit hints or by page-level context. Table 7 summarizes their differences in role framing, objective wording, strategy labels, context rendering, and hint strength. If the neutral prompt still favors boundary-oriented strategies, we treat this as evidence that the preference is not solely induced by explicit structural hints.

Probe	Geom.	Behavior	Key parameters	Placement $\mathcal{T}$
P1 (horiz. crease)	line	inject	$w \in [1, 10], l_r \in [0.5, 1.0]$	a/c/r
P2 (vert. crease)	line	inject	$w \in [1, 10], l_r \in [0.5, 1.0]$	a/c/r
P3 (circular overlay)	disk	blend	$r \in [30, 90], \alpha \in [0.2, 1.0]$	a/c/r
P4 (rect. modification)	rect	erase	$a \in [3\%, 25\%], \beta \in [0.2, 1.0]$	c/b
P5 (thin horiz. line)	line	inject	$w \in [1, 5], l_r \in [0.2, 0.8]$	b/c/r
P6 (gradient band)	line+grad	blend	$\alpha \in [0.05, 0.4], w \in [2, 10]$	a
P7 (dot cluster)	points	inject	$n \in [10, 100], r \in [1, 4], \sigma \in [10, 50]$	a
P8 (irregular patch)	blob	blend	$r_b \in [30, 80], \epsilon \in [0.1, 0.5], \alpha \in [0.3, 0.7]$	r
P9 (diag. crease)	line	inject	$\theta \in [20^\circ, 70^\circ], w \in [1, 6]$	a

Table 6: Probe catalog and parameter ranges. Placement codes a/c/r/b denote anchor/content/random/bridge.



Figure 5: Representative visual examples of the probe families used in the controlled perturbation space.

## B Diagnostic Metrics, Matching, and Terminal Evaluation

### B.1 Exposure Descriptor Definitions

This subsection gives the operational definitions of the five exposure descriptors used in Section 4.4.2. Let  $S(P)$  denote the perturbation mask induced by probe configuration  $P$ , and let  $(W, H)$  be the page size. For annotated layout elements  $L$ , we define the annotated layout support and boundary support as

$$\begin{aligned} \Omega_L &= \bigcup_{\ell \in L} b(\ell), \\ M_{\partial L} &= \mathcal{D} \left( \bigcup_{\ell \in L} \partial b(\ell), \delta \right) \setminus \Omega_L^{\text{erode}(\delta)}. \end{aligned} \quad (29)$$

The five descriptors are computed as

$$\begin{aligned} \text{TOR}(P) &= \frac{|S(P)|}{W \times H}, \\ \text{ACR}(P, L) &= \frac{|S(P) \cap \Omega_L|}{|\Omega_L|}, \\ \text{BPO}(P, L) &= \frac{|S(P) \cap M_{\partial L}|}{|M_{\partial L}|}, \\ \text{BOC}(P, L) &= \frac{|\{\ell \in L : b(\ell) \cap S(P) \neq \emptyset\}|}{|L|}, \\ \text{EIR}(P, E) &= \frac{|\{e \in E : b(e) \cap S(P) \neq \emptyset\}|}{|E|}. \end{aligned} \quad (30)$$

TOR and EIR are output-derived, whereas ACR, BPO, and BOC are annotation-dependent benchmark diagnostics. For BOC and EIR, the intersection predicate is satisfied when at least one pixel of the bounding box overlaps the probe mask (overlap\_px=1).

### B.2 Output Matching and TextSim

Each clean element  $e \in E$  is assigned a candidate counterpart in the perturbed output by maximum-

Dimension	LLM-biased	LLM-neutral
System role	Expert adversarial tester for DLA	QA analyst for robustness
Objective	Max parsing disruption (merge/split/miss)	Test model response to degradation
Strategy labels	bridge/anchor/content/random	between/edge/inside/anywhere
Context source	to_text_description() with gap info	to_neutral_description() coords only
Hint strength	Explicit spatial guidance	Minimal; no structural cues

Table 7: Controlled prompt-pair design for testing structural targeting preference.

IoU lookup:

$$m(e) = \arg \max_{e' \in E_{\text{adv}}} \text{IoU}(e, e'). \quad (31)$$

Ties are broken by adversarial-element index, and no one-to-one Hungarian assignment is enforced. This allows multiple clean elements to map to the same perturbed element, which is necessary for detecting merge-type topology failures.

A match is accepted only when both the geometry and text gates are satisfied:

$$\text{IoU}(e, m(e)) \geq \tau_{\text{iou}}, \quad \text{TextSim}(e, m(e)) \geq \tau_{\text{text}}. \quad (32)$$

We use  $\tau_{\text{iou}} = 0.1$  and  $\tau_{\text{text}} = 0.5$  in all experiments; their rationale and sensitivity are discussed in Appendix B.5.

Text consistency is computed by character-level longest common subsequence:

$$\text{TextSim}(a, b) = \frac{|\text{LCS}(a, b)|}{\max(|a|, |b|)}. \quad (33)$$

Before computing TextSim, we strip leading/trailing whitespace and case-fold to lowercase; internal whitespace is preserved, and no punctuation removal or tokenization is applied. TextSim is used only as a matching criterion for B-SLR, not as the CER computation itself.

### B.3 Canonical Label Mapping

Table 8 reports the label normalization used for detection evaluation and category-level diagnostics. Raw dataset and parser labels are mapped to the five canonical layout categories  $\mathcal{C}_5 = \{\text{text}, \text{title}, \text{table}, \text{figure}, \text{equation}\}$ ; non-content labels are ignored for mAP.

### B.4 Terminal Metric Definitions

We instantiate the terminal component  $\Delta$  through OCR and detection degradation:

$$\Delta = (\Delta_{\text{ocr}}, \Delta_{\text{det}}), \quad (34)$$

where  $\Delta_{\text{ocr}}$  is measured by CER and  $\Delta_{\text{det}}$  by the per-image mAP@0.5 drop.

For the OCR channel, we use character error rate (CER) as the primary terminal judge. Because the audit compares clean and perturbed parser outputs, the clean parser text serves as the reference text for each matched element. Using the maximum-IoU correspondence defined in Appendix B.2, let  $r_e = \text{txt}(e)$  and  $h_e = \text{txt}(m(e))$ . The element-

wise CER is

$$\text{CER}_e(e) = \begin{cases} \frac{d_{\text{Lev}}(r_e, h_e)}{|r_e|}, & \text{IoU}(e, m(e)) > 0, \\ 1, & \text{otherwise,} \end{cases} \quad (35)$$

where the second case represents total text loss when no perturbed element overlaps the clean element. Here  $d_{\text{Lev}}$  denotes character-level Levenshtein distance after stripping leading/trailing whitespace and case-folding to lowercase.

Let

$$E_{\text{text}} = \{e \in E \mid \text{txt}(e) \neq \epsilon\} \quad (36)$$

denote the subset of clean elements with non-empty text. The page-level mean CER is

$$\overline{\text{CER}} = \frac{1}{|E_{\text{text}}|} \sum_{e \in E_{\text{text}}} \text{CER}_e(e), \quad (37)$$

with  $\overline{\text{CER}} = 1$  when  $|E_{\text{text}}| = 0$ .

For the detection channel, we compute per-image mean Average Precision at IoU threshold 0.5:

$$\text{mAP} = \frac{1}{|\mathcal{C}|} \sum_{c \in \mathcal{C}} \text{AP}_c, \quad (38)$$

where  $\mathcal{C} \subseteq \mathcal{C}_5$  is the set of normalized layout classes present in the page-level ground truth. The raw mAP is a detection quality score, so we use its clean-to-perturbed drop as the detection degradation signal:

$$\Delta_{\text{det}} := \Delta \text{mAP} = \text{mAP}(\mathcal{Y}, E) - \text{mAP}(\mathcal{Y}, E_{\text{adv}}). \quad (39)$$

Positive  $\Delta \text{mAP}$  indicates detection degradation, while negative values indicate an incidental mAP improvement after perturbation. CER remains the primary terminal judge for OCR-oriented failure propagation.

### B.5 Operational Constants and Threshold Rationale

**Coverage ratio  $\rho$ .** The coverage ratio

$$\rho(e, S(P)) = \frac{|b(e) \cap S(P)|}{|b(e)|} \quad (40)$$

measures the fraction of an element box directly covered by the perturbation mask. A structurally failed element with  $\rho(e, S(P)) \geq \eta_{\text{occ}}$  is assigned to the direct-occlusion subset  $\mathcal{U}_{\text{miss}}$ ; otherwise, it is assigned to the topology-dominant subset  $\mathcal{U}_{\text{topo}}$ .

**Alignment threshold rationale.** The IoU threshold  $\tau_{\text{iou}} = 0.1$  is intentionally permissive because the IoU gate is used for diagnostic alignment rather

Source family	Raw label(s)	Canonical target	Used in mAP
PubLayNet GT	Text; List	text	yes
PubLayNet GT	Title	title	yes
PubLayNet GT	Table	table	yes
PubLayNet GT	Figure	figure	yes
DocLayNet GT	Caption; Footnote; List-item	text	yes
DocLayNet GT	Section-header	title	yes
DocLayNet GT	Picture	figure	yes
DocLayNet GT	Formula	equation	yes
Parser / MinerU output	figure_caption; table_caption; reference; list; plain_text; table_footnote; formula_caption; index; normal_text	text	yes
Parser / MinerU output	image	figure	yes
Parser / MinerU output	formula; isolate_formula; embedding; isolated	equation	yes
Canonical passthrough	text; title; table; figure; equation	identity	yes
Non-content labels	Page-header; Page-footer; header; footer; abandon; seal	None	no
Fallback rule	Any unseen label	text (default)	yes

Table 8: Label normalization from raw dataset/parser labels to the five canonical layout categories used for detection evaluation.

Symbol	Value	Role	Code reference
$\tau_{\text{iou}}$	0.1	IoU gate for output matching	calculate_b_slr()
$\tau_{\text{text}}$	0.5	TextSim gate for textual identity	calculate_b_slr()
$\eta_{\text{occ}}$	0.3	Occlusion threshold for miss/topo split	_elem_is_occluded()
$\delta$	5 px	Boundary-mask dilation radius	compute_anchor_mask()
overlap <sub>px</sub>	1 px	BOC/EIR box-intersection threshold	compute_boc()

Table 9: Operational constants fixed across all experiments.

than detection-quality scoring. Unlike standard detection evaluation, where IoU thresholds such as 0.5 determine whether a detection is correct, our matching stage only admits a candidate perturbed element for subsequent identity checking. A strict IoU gate would prematurely mark spatially displaced but still identifiable counterparts as lost, thereby conflating geometric displacement with structural disappearance. This follows the spirit of text-aware detection evaluation, where geometric matching can be relaxed when text-level consistency provides the substantive quality signal (Lee et al., 2019; Baek et al., 2020). The TextSim threshold  $\tau_{\text{text}} = 0.5$  requires at least half of the character-level LCS-normalized content to be preserved; below this value, textual identity is treated as structurally lost. Both thresholds are fixed across all parsers, probes, and policies.

## B.6 B-SLR Decomposition Algorithm

Algorithm 1 gives the implementation-level procedure used to decompose B-SLR into direct-occlusion and topology-dominant components. Within the topology-dominant subset  $\mathcal{U}_{\text{topo}}$ , failures are further assigned to three mutually exclusive categories under a fixed priority order: MERGE, MISCLASS, and DEGRADED. MERGE captures multiple clean elements assigned to the same perturbed prediction; MISCLASS captures retained spa-

tial correspondence with a changed canonical category; and DEGRADED covers the remaining non-occluded failures, including text degradation without direct physical coverage.

## C Experimental Protocol and Configuration Details

### C.1 Auditing Protocol Overview and Identifier Convention

Table 10 summarizes the configuration groups used in our experiments. We use A01–A22 for fixed standard configurations, NT01–NT07 for EIR-targeted configurations, and S01–S13 for randomized sweep configurations. For compact reporting, each fixed configuration is encoded as

$$P_n \cdot t[\xi], \quad (41)$$

where  $P_n$  identifies the probe family in Table 6,  $t \in \{\text{a}, \text{c}, \text{r}, \text{b}\}$  denotes placement, and  $\xi$  records the dominant varied parameter. Tables 11, 12, and 13 provide the full decoding.

### C.2 Phase 1 Fixed Configurations

Table 11 decodes the 22 standard Phase 1 configurations. These configurations are used to profile probe-level effects under controlled parameter and placement choices.

---

**Algorithm 1: Decomposed B-SLR classification.**

---

**Input:**  $E, E_{\text{adv}}, S(P)$ **Output:**  $\text{SLR}_{\text{miss}}, \text{SLR}_{\text{topo}}$ , per-category counts

```
1 Compute
   $m(e) = \arg \max_{e' \in E_{\text{adv}}} \text{IoU}(e, e')$  for
  each  $e \in E$ 
2 Count how many clean elements map to
  each perturbed prediction
3 foreach  $e \in E$  do
4    $\hat{e} \leftarrow m(e)$ 
5    $\hat{l} \leftarrow \text{IoU}(e, \hat{e})$ 
6   if  $\hat{l} < \tau_{\text{iou}}$  then
7     if  $\rho(e, S(P)) \geq \eta_{\text{occ}}$  then MISS
8     else DEGRADED
9   else if multiple clean elements map to  $\hat{e}$ 
     then
10    MERGE
11   else if  $c(e) \neq c(\hat{e})$  then
12    MISCLASS
13   else if  $\text{txt}(e) \neq \epsilon$  and
      $\text{TextSim}(e, \hat{e}) < \tau_{\text{text}}$  then
14    if  $\rho(e, S(P)) \geq \eta_{\text{occ}}$  then MISS
15    else DEGRADED
16   else INTACT
17 end
18  $\text{SLR}_{\text{miss}} \leftarrow n_{\text{MISS}}/|E|$ 
19  $\text{SLR}_{\text{topo}} \leftarrow$ 
    $(n_{\text{MERGE}} + n_{\text{MISCLASS}} + n_{\text{DEGRADED}})/|E|$ 
```

---

Protocol	Configs	Per config	Goal
Phase 1 fixed	29	1,000 imgs	probe effect profiling
Phase 1 sweep	13	1,000 imgs	randomized-parameter check
Phase 2 policies	5 policies	1,000 imgs	targeting-policy comparison

---

Table 10: Overview of auditing protocols and configuration groups.

### C.3 EIR-Targeted NT Configurations

The NT series uses iterative multi-stamp placement to reach target element-interference levels. The target  $\tau$  specifies the intended fraction of clean elements whose boxes overlap the probe mask at injection time.

### C.4 Randomized Sweep Configurations

In addition to the fixed Phase 1 matrix, we run randomized sweeps to test whether structural-exposure signals persist when probe parameters vary stochas-

---

Label	Probe tuple label	Key parameters	Purpose
A01	$P_1 \cdot a[w1]$	$w = 1, l = W$	P1 lower bound
A02	$P_1 \cdot a[w8]$	$w = 8, l = W$	P1 upper bound
A03	$P_2 \cdot a[w1]$	$w = 1, l = H$	P2 lower bound
A04	$P_2 \cdot a[w8]$	$w = 8, l = H$	P2 upper bound
A05	$P_3 \cdot a[\alpha.3]$	$r = 60, \alpha = 0.3$	stamp faint
A06	$P_3 \cdot a[\alpha.1]$	$r = 60, \alpha = 1.0$	stamp opaque
A07	$P_4 \cdot c[5\%]$	$a = 5\%, \beta = 0.3$	erasure mild
A08	$P_4 \cdot c[20\%]$	$a = 20\%, \beta = 1.0$	erasure severe
A09	$P_5 \cdot b[w1]$	$w = 1, l = 0.5W$	separator thin
A10	$P_5 \cdot b[w3]$	$w = 3, l = 0.5W$	separator thick
A11	$P_6 \cdot a[\alpha.1]$	$\alpha = 0.1, w = 5$	ghost imperceptible
A12	$P_6 \cdot a[\alpha.3]$	$\alpha = 0.3, w = 5$	ghost visible

---

*Placement control groups*  
(matched probe, varying  $\mathcal{T}$ ):

---

A13	$P_1 \cdot c[w3]$	$w = 3, l = W$	crease on text
A14	$P_1 \cdot r[w3]$	$w = 3, l = W$	crease random
A15	$P_3 \cdot c[\alpha.5]$	$r = 60, \alpha = 0.5$	stamp on text
A16	$P_3 \cdot r[\alpha.5]$	$r = 60, \alpha = 0.5$	stamp random
A17	$P_5 \cdot c[w2]$	$w = 2, l = 0.5W$	sep. on text
A18	$P_5 \cdot r[w2]$	$w = 2, l = 0.5W$	sep. random
A19	$P_4 \cdot b[20\%]$	$a = 20\%, \beta = 1.0$	erasure bridge
A20	$P_5 \cdot c[w3]$	$w = 3, l = 0.5W$	sep. extended
A21	$P_3 \cdot a[\alpha.5]$	$r = 60, \alpha = 0.5$	stamp anchor
A22	$P_1 \cdot a[w3]$	$w = 3, l = W$	crease anchor

---

Table 11: Phase 1 fixed configurations under the A01–A22 identifier convention. Tuple labels decode probe family, placement, and dominant parameter;  $W/H$  denote page width/height.

---

Label	Probe tuple label	Target $\tau$	Method
NT01	NT[.05]	0.05	targeted stamp placement
NT02	NT[.10]	0.10	targeted stamp placement
NT03	NT[.20]	0.20	targeted stamp placement
NT04	NT[.35]	0.35	targeted stamp placement
NT05	NT[.50]	0.50	targeted stamp placement
NT06	NT[.70]	0.70	targeted stamp placement
NT07	NT[1.0]	1.00	targeted stamp placement

---

Table 12: EIR-targeted configurations under the NT01–NT07 identifier convention. The probe family and placement mechanism are fixed; only the target interference ratio  $\tau$  varies.

tically. Table 13 lists the randomized configurations. Paired configurations share sampled geometry, appearance, and behavior parameters while varying only placement.

### C.5 Inference, Randomness, and Software

**Randomness control.** All experiments use `numpy.random.default_rng(seed=42)` as the base random generator. The randomized-sweep paired configurations use deterministic per-image seeds  $(\text{image\_index} + 1) \times 10^5 + \text{pair\_id}$  so that  $\mathcal{H}$ ,  $\mathcal{V}$ , and  $\mathcal{B}$  are sampled identically across paired placement strategies while only  $\mathcal{T}$  varies.

ID	Probe	Random parameters	$\mathcal{T}$	Notes
S01	P1	$w \sim U(1, 10)$	anchor	
S02	P2	$w \sim U(1, 10)$	anchor	
S03	P3	$r \sim U(30, 90), \alpha \sim U(0.2, 1)$	anchor	
S04	P4	$a \sim U(3\%, 25\%), \beta \sim U(0.2, 1)$	content	
S05	P5	$w \sim U(1, 5), l \sim U(0.2W, 0.8W)$	bridge	
S06	P6	$\alpha \sim U(0.05, 0.4), w \sim U(2, 10)$	anchor	
S07	P7	$n \sim U(10, 100), r \sim U(1, 4)$	random	
S08	P8	$r_b \sim U(30, 80), \epsilon \sim U(0.1, 0.5)$	anchor	
S09	P9	$\theta \sim U(20, 70), w \sim U(1, 6)$	anchor	
S10	P1	$w \sim U(1, 10)$	content	paired w/ S01
S11	P1	$w \sim U(1, 10)$	random	paired w/ S01
S12	P3	$r \sim U(30, 90), \alpha \sim U(0.2, 1)$	content	paired w/ S03
S13	P3	$r \sim U(30, 90), \alpha \sim U(0.2, 1)$	random	paired w/ S03

Table 13: Randomized sweep configurations. Paired configurations share sampled  $\mathcal{H}$ ,  $\mathcal{V}$ , and  $\mathcal{B}$ ; only  $\mathcal{T}$  varies.

Parameter	LLM policies	VLM policy
Backend	DeepSeek-Chat	Qwen-VL-Max / GPT-4o
Temperature	0.7	0.7
Max tokens	API default	1,024
Response format	json_object	free-form (parsed)
Max retries	3	3
Image long edge	—	1,024 px
JPEG quality	—	85
GPT-4o detail	—	high

Table 14: LLM/VLM inference parameters.

LLM/VLM policies inherit stochasticity from API sampling; all other components are deterministic given the seed.

**Software versions.** We use MinerU v2.7.6 with DocLayout-YOLO, PP-StructureV3 with PaddleOCR 3.4.1 and PaddlePaddle 3.3.1, Python 3.10, NumPy 2.2.6, and OpenCV 4.x.

**Hardware.** GPU experiments used one NVIDIA GeForce RTX 5090 with 32 GiB device memory.

## C.6 Statistical Verification Layers

We use the six verification layers in Table 15 to check that the main conclusions do not depend on a single aggregation view. The main text emphasizes configuration-level analyses, while the remaining layers provide robustness checks against document heterogeneity, nonlinearity, and attack-design confounds.

Layer	Method	Unit	Threat checked
0	Raw OLS	per-image record	baseline association
1	Config-level OLS	29 config means	within-image noise
2	Image fixed effects	de-measured residuals	document heterogeneity
3	Per-image Spearman	per-image $\rho$ + win rate	nonlinearity
4	Dose-response bins	EIR quintile bins	reverse causality
5	Quasi-natural	within-config quartiles	attack-design confound

Table 15: Six-layer statistical verification framework.

Pipeline	Channel	$\mathcal{G}_{\text{area}}$			$\mathcal{G}_{\text{struct}}$	
		TOR	ACR	BPO	BOC	EIR
MinerU	composite	.780	.760	<b>.821</b>	.336	.280
	iou-only	.782	.755	<b>.869</b>	.194	.149
	text-only	<b>.629</b>	.622	.613	.477	.424
PP-V3	composite	.150	.149	.161	<b>.856</b>	.852
	iou-only	.704	.678	<b>.781</b>	.203	.205
	text-only	.017	.018	.017	<b>.738</b>	.733

Table 16: Channel-by-gradient regression breakdown: configuration-level  $R^2$  from univariate OLS fits between each diagnostic descriptor and each B-SLR channel. Bold marks the strongest predictor per row.

## D Additional Results and Robustness Checks

### D.1 Channel-by-Gradient Breakdown

Table 16 expands the gradient analysis in Section 5.2.4 by reporting configuration-level  $R^2$  between each diagnostic descriptor and each B-SLR channel. This breakdown complements Table 4 by showing how the five exposure descriptors relate to composite B-SLR and its IoU-fail and text-fail-only subchannels.

### D.2 Randomized Sweep Robustness

The randomized sweep configurations in Appendix C.4 test whether the structural-exposure signal persists when probe size and appearance vary stochastically rather than being fixed by the Phase 1 matrix. At the configuration level, EIR remains more predictive of B-SLR than footprint-style descriptors:  $R^2(\text{EIR} \rightarrow \text{B-SLR}) = 0.613$  on MinerU and 0.530 on PP-V3, while TOR/ACR/BPO reach at most 0.048 on MinerU and 0.020 on PP-V3. BOC shows the same trend ( $R^2 = 0.591$  on MinerU and 0.532 on PP-V3). Thus, the dominance of structure-count descriptors is not an artifact of hand-selected fixed configurations.

### D.3 Dose-Response Monotonicity

We further check whether structural interference produces a monotonic dose-response in B-SLR. Binning observations by EIR, PP-V3 exhibits strict monotonic growth: mean B-SLR increases from 0.018 in the lowest bin to 0.480 in the highest bin. MinerU also increases monotonically, from 0.025 to 0.181, but with a shallower slope. Within fixed configurations, partitioning images into EIR quartiles yields monotonically increasing B-SLR from Q1 to Q4 in the majority of configurations for both pipelines. Together with the randomized sweep in Section D.2, this supports that the structural-exposure effect is not an artifact of either specific

configuration choices or a single aggregation view.

#### D.4 Downstream Propagation Details

The downstream propagation experiment tests whether parser-level structural loss affects practical document use. We construct 975 extractive QA pairs from clean parser outputs over a 500-page subset. Each QA pair contains a question, a gold answer span, an evidence text span, and the corresponding page identifier. The QA set covers 349 unique pages, with at most four QA pairs per page. The answer types include span answers, titles, numeric answers, and captions.

**Perturbation conditions.** We compare four conditions: clean pages, area-matched erasure (AM), structural probe (Str.), and large-area erasure (LA). AM and Str. have nearly identical footprint, with mean TORs of 0.10% and 0.11%, respectively. LA serves as a large-footprint control with mean TOR 16.61%, roughly 150× larger than the matched-footprint conditions.

**Downstream QA.** For each parser and condition, the parsed page text is serialized as the context for a fixed QA answerer. The answerer is instructed to answer using only the provided parsed text; if the answer is absent, it returns NOT\_FOUND. We report exact-match accuracy (EM), token-level F1, answer-missing rate, and the EM drop from the clean condition. A QA instance is counted as answer-missing when the gold answer string is absent from the parsed page text. Empty parser outputs are retained and counted as incorrect and answer-missing when applicable.

**Page-internal retrieval.** For retrieval, the corpus is restricted to chunks from the QA’s own page under the same parser and perturbation condition. This page-internal setting aligns retrieval with the single-page QA task and isolates whether the perturbed parser output still contains retrievable evidence. We use block-aware chunking with a target length of 400 characters, minimum length 80, maximum length 700, and overlap 80. Two retrieval backends are evaluated: BM25 and a dense encoder based on sentence-transformers/all-MiniLM-L6-v2. For each QA, we retrieve the top 10 chunks.

**Retrieval metrics.** We report two retrieval signals. Evidence Recall@k checks whether any top-k chunk contains the evidence text, while Answer Hit@k checks whether any top-k chunk contains

the gold answer. The main text reports Answer Hit@5 because it directly measures whether the answer-bearing content remains retrievable. We additionally report evidence Recall@5 and evidence MRR@10 in Table 17.

The full retrieval metrics are consistent with the main-text AnsHit@5 results. In the main-text table, BM25 AnsHit@5 and Dense AnsHit@5 refer to Answer Hit@5, i.e., whether any top-5 retrieved chunk contains the gold answer string. Under matched footprint, the structural probe causes much larger retrieval degradation than area-matched erasure across both parsers and both retrieval backends. For example, on MinerU, BM25 evidence R@5 drops from 66.7% under AM to 49.2% under Str., while AnswerHit@5 drops from 93.8% to 81.0%. On PP-V3, the same pattern holds: BM25 evidence R@5 drops from 63.9% to 52.7%, and AnswerHit@5 drops from 92.9% to 83.1%. Thus, the downstream effect is not specific to the QA answerer or to a single retrieval backend.

#### D.5 Policy Pathway Composition

Figure 6 provides the fine-grained pathway composition behind the Phase 2 policy comparison in Table 5. Across policies, topology-dominant components account for most structural loss, while direct-occlusion loss remains small for targeted policies. This corroborates the main-text observation that efficient targeting exposes topology-level vulnerability rather than simply increasing physical coverage.

### E Prompts, Reproducibility, and Scope

#### E.1 Reproducibility Checklist

- **Data:** PubLayNet and DocLayNet validation splits; pages with fewer than five original spans are filtered; the final shared evaluation pool contains 1,000 pages.
- **Pipelines:** MinerU v2.7.6 with DocLayout-YOLO, and PP-StructureV3 with RT-DETR-H and PaddleOCR 3.4.1. Software and hardware details are reported in Appendix C.5.
- **Matching:** maximum-IoU lookup with unified IoU and TextSim gates ( $\tau_{\text{iou}} = 0.1$ ,  $\tau_{\text{text}} = 0.5$ ); no one-to-one Hungarian assignment is enforced.
- **Probes:** P1–P9 with bounded configuration ranges, listed in Table 6.
- **Configurations:** A01–A22 and NT01–NT07 for Phase 1 fixed auditing (Tables 11 and 12);

Parser	Condition	BM25 R@5 <sub>evid</sub>	BM25 MRR@10 <sub>evid</sub>	BM25 AnsHit@5	Dense R@5 <sub>evid</sub>	Dense MRR@10 <sub>evid</sub>	Dense AnsHit@5
MinerU	Clean	68.7	61.6	94.6	67.9	56.9	93.6
	AM	66.7	59.6	93.8	65.7	55.2	92.8
	Str.	49.2	43.3	81.0	48.4	41.2	80.4
	LA	35.6	31.2	58.8	35.4	28.7	59.4
PP-V3	Clean	66.4	59.3	94.7	64.5	53.1	95.1
	AM	63.9	56.9	92.9	62.2	51.2	93.4
	Str.	52.7	46.8	83.1	51.5	41.5	83.5
	LA	32.6	29.2	57.9	31.9	26.8	58.7

Table 17: Additional page-internal retrieval metrics for downstream propagation. All scores are percentages and higher is better. R@5<sub>evid</sub> and MRR@10<sub>evid</sub> use evidence-text containment as the relevance signal, while AnsHit@5 checks whether a top-5 retrieved chunk contains the gold answer.

Pathway decomposition of structural failure (Phase 2,  $n_{img} = 1000$  per policy)

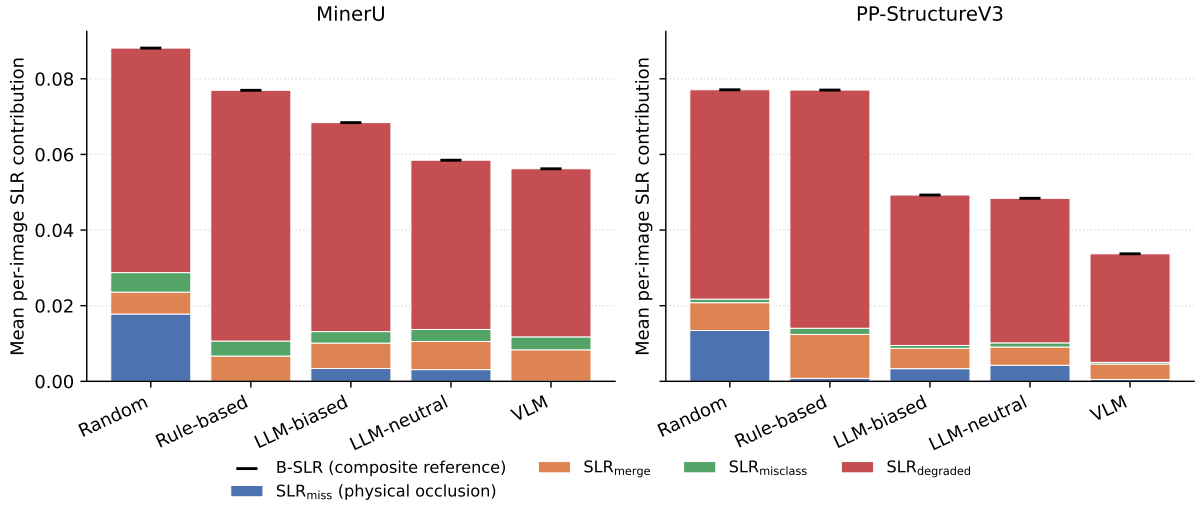


Figure 6: Phase 2 pathway composition of mean per-image structural loss for each policy ( $n=1,000$  pages). Stacks show SLR<sub>miss</sub>, SLR<sub>merge</sub>, SLR<sub>misclass</sub>, and SLR<sub>degraded</sub>; black ticks mark composite B-SLR, and higher stacks indicate greater structural loss.

S01–S13 for randomized sweeps (Table 13); five policy families for Phase 2.

- **Statistics:** six-layer verification protocol, including configuration-level OLS, image fixed effects, per-image rank checks, dose-response bins, and within-configuration quartile checks (Table 15).
- **Randomness:** base seed 42 for deterministic components; paired randomized-sweep configurations use deterministic per-image seeds; LLM/VLM policies inherit stochasticity from API sampling.
- **Key output columns:** image\_id, config\_id, TOR, ACR, BPO, BOC, EIR, B\_SLR, B\_SLR\_iou\_only, SLR\_miss, SLR\_topo, CER\_matched\_mean, mAP\_clean, mAP\_adv, delta\_mAP, and n\_orig\_spans.
- **Metrics:**  $\overline{\text{CER}}$  is the primary terminal OCR judge; per-image mAP@0.5 over the five canonical layout classes defines the supplementary detection-channel drop  $\Delta\text{mAP}$ .

## E.2 Prompt Templates

The policy prompts are designed to emit the same output schema: a probe type, bounded probe parameters, and a placement strategy. The biased and neutral LLM variants differ in role framing, objective wording, strategy labels, and context rendering, as summarized in Table 7. Figure 7 shows abridged prompt excerpts for the three prompt-based policy variants. For the text-only policies, the biased variant uses a structure-aware page description through `context.to_text_description()`, whereas the neutral variant uses a coordinate-only rendering through `context.to_neutral_description()`. The VLM policy instead receives the raw page image and predicts only the probe type and placement strategy.

If a returned strategy is unrecognized, the fallback is random; if the probe type is invalid, the fallback is P5.

### (a) LLM-biased prompt excerpt

You are an expert adversarial tester for Document Layout Analysis (DLA) systems.

Your goal is to choose ONE visual probe and place it on the document image to cause maximum parsing failure, such as merging, splitting, or missing layout blocks.

Available probe types: P1-P9.

Placement strategies: bridge / anchor / content / random.

Output strictly valid JSON.

*Context:* structure-aware page description with block coordinates, gap information, and candidate vulnerable regions.

### (b) LLM-neutral prompt excerpt

You are a quality assurance analyst evaluating the robustness of Document Layout Analysis (DLA) systems.

Select ONE visual perturbation probe and one placement strategy to test how the model responds to realistic document degradation.

Placement options: between / edge / inside / anywhere.

Output strictly valid JSON.

*Context:* coordinate-only page description with block types and bounding boxes, without explicit structural vulnerability hints.

### (c) VLM strategy-only prompt excerpt

Look at this document image carefully. Observe the text blocks, figures, tables, and whitespace regions.

Based only on what you see in the image, select a probe type and a placement strategy.

Placement options: between / edge / inside / anywhere.

The system will automatically determine exact placement coordinates based on the chosen strategy.

Output strictly valid JSON.

*Input:* raw page image only; no coordinate text description is provided.

Figure 7: Abridged prompt templates for the prompt-based policy variants. All prompts emit the same output schema, while differing in role framing and available context. For the neutral and VLM prompts, strategy names are mapped internally as between→bridge, edge→anchor, inside→content, and anywhere→random.

## E.3 Context Encoder for Non-VLM Policies

For random, rule-based, and LLM-based policies, the context encoder provides three groups of page-level features:

- **Visual statistics:** grayscale moments, edge density, and page size.
- **Layout structure:** block count, category entropy, and area distribution.
- **Spatial relations:** gap density, nearest-neighbor spacing, and multi-column cues.

The biased prompt uses a structure-aware text rendering through `to_text_description()`, while the neutral prompt uses a coordinate-only rendering through `to_neutral_description()`.